Mon. Not. R. Astron. Soc. **000**, 000–000 (0000) Printed 24 March 2015 (MN LaTeX style file v2.2)

arXiv:1503.06373v1 [astro-ph.CO] 22 Mar 2015

Detection of a filament connected to CL0016 with weak gravitational lensing

Yuichi Higuchi[1⋆], Masamune Oguri[2,3,4], Masayuki Tanaka[5] and Junya Sakurai[5,6]
[1] *Astronomy Data Center, National Astronomical Observatory of Japan, 2-21-1 Osawa, Mitaka, Tokyo 181-8588, Japan*
[2] *Research Center for the Early Universe, University of Tokyo, 7-3-1 Hongo, Bunkyo-ku, Tokyo 113-0033, Japan*
[3] *Department of Physics, University of Tokyo, 7-3-1 Hongo, Bunkyo-ku, Tokyo 113-0033, Japan*
[4] *Kavli Institute for the Physics and Mathematics of the Universe (Kavli IPMU, WPI), University of Tokyo, Chiba 277-8583, Japan*
[5] *Optical and Infrared Astronomy Division, National Astronomical Observatory of Japan, 2-21-1 Osawa, Mitaka, Tokyo 181-8588, Japan*
[6] *Department of Astronomical Science, SOKENDAI(The Graduate University for Advanced Studies), Mitaka, Tokyo, 181-8588, Japan*

24 March 2015

ABSTRACT

We report on the weak lensing detection of a filament between two galaxy clusters at $z = 0.55$, CL0015.9+1609 and RX J0018.3+1618. We conduct weak lensing analysis of deep multi-band Subaru/Suprime-Cam images with *Lensfit*. The weak lensing signals from the filament are contaminated by signals from the adjacent massive clusters and we statistically subtract the cluster component using two different methods. Both methods yield consistent shear profiles on the filament with $\gtrsim 2\sigma$ significance and the average surface mass density of the filament is $\langle\Sigma\rangle = (3.20 \pm 0.10) \times 10^{14} h$ $\mathrm{M}_\odot \mathrm{Mpc}^{-2}$, which is in broad agreement with previous studies. On-going surveys such as Hyper Suprime-Cam will identify more filaments, which will serve as a new probe of structure formation in the Universe.

Key words: gravitational lensing: weak, large-scale structure of Universe
LaTeX – style files: `mn2e.sty`

1 INTRODUCTION

Recent observations have revealed that the Universe is dominated by unknown components called dark matter and dark energy (Hinshaw et al. 2013; Rest et al. 2014; Planck Collaboration et al. 2015). The theoretical model called Λ Cold Dark Matter (ΛCDM) model, which contains these components, has been confronted with several observational tests such as correlation functions (e.g., Blake & Bridle 2005; Tegmark et al. 2006; Hütsi 2006; Marín et al. 2013) and Minkowski functionals (e.g., Hikage et al. 2008; Petri et al. 2013). These statistical observables are in excellent agreement with theoretical predictions from the ΛCDM model. However, these tests only use ensemble average properties of the matter distribution. Complementary tests can be done with voids and filaments, which are important constitutes of the large-scale structure of the Universe. Voids are underdense regions whose properties have been studied theoretically (e.g., Furlanetto & Piran 2006; Kamionkowski et al. 2009; Higuchi et al. 2013; Krause et al. 2013; Sutter et al. 2015). On the other hand, filaments are slightly overdense regions connecting massive haloes.

Large N-body simulations indicate that filaments are formed in the process of merging and accretion (Bond et al. 1996; Springel 2005; Colberg et al. 2005). Therefore, filaments affect properties of nearly haloes. The properties of haloes residing with filaments are well studied through N-body simulations (Codis et al. 2012; Aragon-Calvo & Yang 2014; Higuchi et al. 2014). In order to find such filamentary structures, a variety of algorithms have been developed (Martinez & Saar 2002; Sheth & Jain 2003; Sousbie et al. 2006; Mead et al. 2010).

Although we can see cosmic web in simulations, filamentary structures are hard to be detected observationally due to their low overdensity (Sousbie et al. 2008; Heymans et al. 2008; Clampitt et al. 2014). Some studies claimed the detection of filaments with X-ray (Briel & Henry 1995; Tittley & Henriksen 2001; Fang et al. 2002; Durret et al. 2003; Werner 2008), although it is difficult to distinguish whether those signals come from filaments or from haloes at the edge of the filaments.

While X-ray probes only hot intergalactic medium, weak gravitational lensing can probe not only baryon but also dark matter which occupies a dominant part of a filament

---

[⋆] E-mail: yuichi.higuchi@nao.ac.jp

© 0000 RAS

mass. However, the detection of filaments with weak lensing have not been very successful. While weak lensing detections of filaments between clusters have been claimed (e.g., Clowe et al. 1998; Kaiser et al. 1998; Gray et al. 2002; Dietrich et al. 2004), it has also been suggested that these detection signals might have come from systematics of the analysis (Gavazzi et al. 2004; Heymans et al. 2008). Recently more secure detections of filaments with weak gravitational lensing have been reported in the systems Abell 222/223 (Dietrich et al. 2012) and MACSJ0717.5+3745 (Jauzac et al. 2012). However, a lager sample is needed in order to test the ΛCDM model with large-scale structures, and also to investigate observational properties of filaments. In this paper, we report the new detection of a filament with weak gravitational lensing.

This paper is organized as follows. In Section 2, we describe the lensing analysis methods with a focus on the basics of weak lensing and halo properties. In Section 3, we describe our data analysis method, including the selection of background galaxies, the lensing analysis with *Lensfit*, the reconstruction of the filament mass distribution and the evaluation of contaminations from clusters. In Section 4, we show the results of lensing analysis. We summarize our result in Section 5.

In this paper, cosmological parameters are set according to the result of the Planck satellite (Planck Collaboration et al. 2013); Hubble constant $H_0 = 67.3$ km/s/Mpc, cosmological constant $\Omega_m = 0.315$, dark energy $\Omega_\Lambda = 0.685$.

2 THEORIES FOR WEAK LENSING

First, we summarize the theory of weak gravitational lensing. We follow the formalism outlined in Bartelmann & Schneider (2001).

2.1 Estimation of lensing signals from images

Weak lensing signals are obtained from observed galaxy ellipticities. However, convergence $\kappa(\theta)$ and shear $\gamma(\theta)$ are not directly related to galaxy ellipticities. The galaxy ellipticity of a lensed object depends on the reduced shear g defined as

$$\mathrm{g}(\boldsymbol{\theta}) = \frac{\gamma(\boldsymbol{\theta})}{1-\kappa(\boldsymbol{\theta})}. \tag{1}$$

In the weak lensing limit, the reduced shear is related to the galaxy ellipticity ε as

$$\varepsilon \sim \varepsilon^{\mathrm{s}} + \mathrm{g}, \tag{2}$$

where ε^{s} is an intrinsic ellipticity of the galaxy. On the basis of the cosmological principle, we can assume that orientations of galaxies are random, i.e., the ensemble average of intrinsic ellipticities should be zero. Therefore, the average observed ellipticity is related to reduced shear as

$$\langle\varepsilon\rangle = \langle \mathrm{g}\rangle \sim \langle\gamma\rangle, \tag{3}$$

where $\langle\cdots\rangle$ indicates ensemble average in a bin.

We need to calculate the lensing depth of source galaxies in order to estimate physical quantities such as cluster masses from weak lensing signals. The lensing amplitude is proportional to the distance ratio averaged over the population of source galaxies,

$$\left\langle \frac{\mathrm{D_{ls}}}{\mathrm{D_s}} \right\rangle = \int \mathrm{d}z \frac{\mathrm{dp}}{\mathrm{d}z}\frac{\mathrm{D_{ls}}}{\mathrm{D_s}}, \tag{4}$$

where $\mathrm{D_{ls}}$ and $\mathrm{D_s}$ are the angular diameter distances from the lens to the source and from the observer to the source, respectively. $\mathrm{dp}/\mathrm{d}z$ is the probability distribution function of redshifts of source galaxies. The critical projected mass density is described with the lensing amplitude as

$$\Sigma_{\mathrm{cr}} = \frac{\mathrm{c}^2}{4\pi \mathrm{G}}\mathrm{D_l}^{-1}\left\langle \frac{\mathrm{D_{ls}}}{\mathrm{D_s}} \right\rangle^{-1}, \tag{5}$$

where c is speed of light and G is gravitational constant. In this paper, we assume that all galaxies are located at this distance.

2.2 Model of filament profile

The filament profile has been studied through both simulations and observations (Colberg et al. 2005; Dietrich et al. 2012; Higuchi et al. 2014). These studies showed that the convergence profile of filaments is described as a function of distance θ from the line which connects between haloes on the sky plane (hereafter halo-halo axis) as (Colberg et al. 2005)

$$\kappa(\theta) = \frac{\kappa_0}{1+(\theta/\theta_c)^2}, \tag{6}$$

where κ_0 describes the convergence value at $\theta = 0$ and θ_c is the scale length of a filament. For spherically symmetric objects, it is common to use reduced shear values defined relative to the centre of objects as

$$\begin{pmatrix} \mathrm{g}_+ \\ \mathrm{g}_\times \end{pmatrix} = \begin{pmatrix} -\cos 2\phi & -\sin 2\phi \\ -\sin 2\phi & \cos 2\phi \end{pmatrix} \begin{pmatrix} \mathrm{g}_1 \\ \mathrm{g}_2 \end{pmatrix}, \tag{7}$$

where ϕ is the angle between axis-θ_1 and $\boldsymbol{\theta}$. g_+ and $\mathrm{g}_\times$ are tangential and cross reduced shear components, respectively. However, filaments are more like axial symmetric. Therefore following Higuchi et al. (2014), for filaments we define the ”tangential shear” at each point as g_+ relative to the closest point on the halo-halo axis to the point. In this definition, the tangential shear profile of filaments takes negative values near the halo-halo axis and positive values at large radii (see Section 3.2).

2.3 NFW profile

Weak lensing signals from filaments are contaminated by signals from nearby clusters. We estimate the effect from clusters by using the cluster mass profile, referred as the Navarro, Frenk and White (hereafter NFW) model (Navarro et al. 1997), which has well been studied in simulations and observations (Gao et al. 2008; Okabe et al. 2010; Oguri et al. 2012). These studies indicate that the three-dimensional mass profile of clusters declines as r^{-1} inside the scale r_s and de- clines as r^{-3} outside r_s. The NFW profile is described as

$$\rho(\mathrm{r}) = \begin{cases} \frac{\rho_s}{r/r_s(1+r/r_s)^2} & (r < r_{\mathrm{vir}}) \\ 0 & \mathit{otherwise}, \end{cases} \tag{8}$$

where r_s and $r_{\rm vir}$ are the scale radius and virial radius, respectively. The characteristic density ρ_s is defined as

$$\rho_s = \frac{\Delta_{\rm vir}(z)\bar{\rho}(z)c_{\rm vir}^3}{3\left[\ln\left(1+c_{\rm vir}\right) - c_{\rm vir}/\left(1+c_{\rm vir}\right)\right]}, \tag{9}$$

where $\Delta_{\rm vir}(z)$ is the non-linear overdensity predicted by the spherical collapse model. We parametrize the mass profile with two parameters. One is the concentration parameter:

$$c_{\rm vir} = \frac{r_{\rm vir}}{r_s}, \tag{10}$$

and the other is the virial mass:

$$M_{\rm vir} = \frac{4\pi}{3}\Delta_{\rm vir}\left(z\right)\bar{\rho}(z)r_{\rm vir}^3. \tag{11}$$

The analytical lensing profile of the NFW profile is well studied (see Wright & Brainerd 2000). In order to constrain the cluster density profiles, we fit the lensing signals with the two fitting parameters $c_{\rm vir}$ and $M_{\rm vir}$ by minimizing a chi-square value defined as

$$\chi^2 = \sum_i \frac{\{g_{+,{\rm im}}(\theta_i) - g_{+,{\rm ana}}(\theta_i)\}^2}{\sigma^2_{g_{+,{\rm im}}}}, \tag{12}$$

where $g_{+,{\rm im}}(\theta_i)$ and $g_{+,{\rm ana}}(\theta_i)$ are circular-averaged tangential shear values at i-th bin estimated from data and model, respectively, and $\sigma_{g_{+,{\rm im}}}$ is dispersion in i-th bin estimated from data.

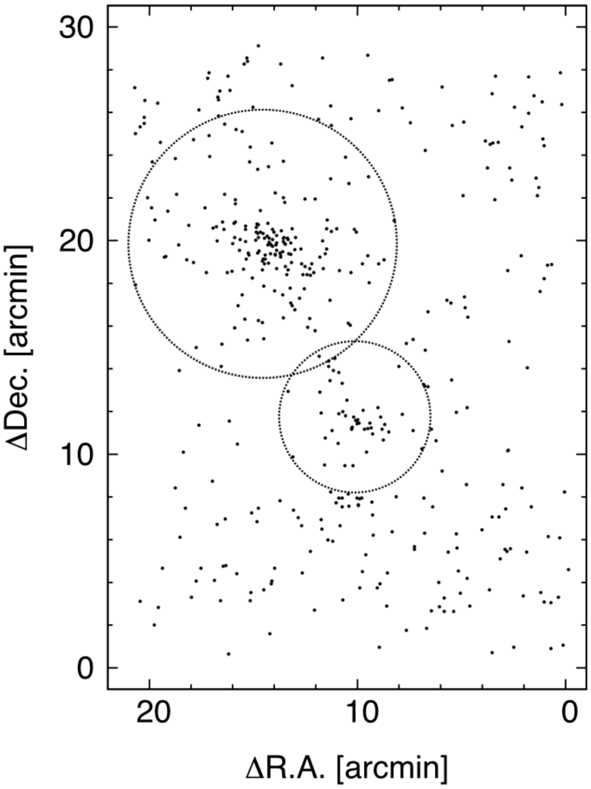

Figure 1. Galaxy distributions at the cluster redshift. The filled points show galaxies in the photometric redshift range between $0.5 < z_{\rm photo} - \sigma$ and $z_{\rm photo} + \sigma < 0.6$ where σ is the photo-z estimation error. The circles show the viral radii of two clusters estimated from profile fitting in Section 3.

3 DATA AND ANALYSIS METHOD

In this section, we summarize the data, weak lensing analysis methods and the methods for subtracting the cluster components.

3.1 Data reduction

We analyze the mass distribution around CL0015.9+1609 (hereafter CL0016) and RX J0018.3+1618 (hereafter RX J0018) at redshift $z = 0.55$ (Connolly et al. 1996; Kodama et al. 2005; Tanaka et al. 2005, 2009). These previous studies show that the galaxy distribution between these two clusters exhibit filamentary structure (see Figure 1). In the paper, we use the data taken with the Subaru Prime Focus Camera (Suprime-Cam; Miyazaki et al. 2002) mounted on the Subaru Telescope during the nights of 2003 September 25-26 (Kodama et al. 2005; Tanaka et al. 2005). We retrieve these data from the data archive system, SMOKA (Baba et al. 2002). The field of view of the Suprime-Cam is 34×27 arcmin^2 with the pixel scale of 0.20 arcsec. It is observed through several broad-band filters ($BVRi'z'$) down to limiting magnitude $B = 26.9$, $V = 26.2$, $R = 26.0$, $i' = 25.9$ and $z' = 24.6$, respectively. The seeing size is about 0″.65 (FWHM). For more details, see Kodama et al. (2005) and Tanaka et al. (2005).

The data are reduced with a modified version of the LSST stack, following the standard procedures of bias subtraction, flat-fielding, distortion correction, sky subtraction and coadding to generate the stacked image from the mosaic images. The flat frames are constructed with the dithered science frames. The MAG_AUTO in SExtractor is used as a measure of the total magnitude (Bertin & Arnouts 1996).

For weak lensing analysis, a precise PSF model is crucial and we select PSF reference stars as follows. Objects are detected in the stacked i'-band image by using SExtractor. We use the same detection criteria used in Kodama et al. (2005). Stars are then selected in a standard way by identifying the stellar sequence in magnitude $m_{i'}$ vs half light radius r_h plane. To be specific, we apply $20.5 \leqslant m_i' \leqslant 23.5$, $r_h \leqslant 0.75$ arcsec and more than 20σ above the median sky. In addition, STAR_CLASS$\geqslant$0.95 and FLAG$=0$ in SExtractor are also imposed. We set the fifth oder polynomial coefficients to fit the spatial variation of PSFs. For calculating the astrometric shifts between different shots, stars with 20σ are used.

Since contaminations by galaxies near the cluster redshift dilute weak lensing signals, for weak lensing analysis we select only background galaxies using photometric redshifts. We use the photometric redshift catalog constructed in Tanaka et al. (2005) with the photometric redshift code of Kodama et al. (1999). Specifically, galaxies in photometric redshift range $z_{\rm photo} - \sigma \geqslant 0.6$ are selected as background galaxies based on the photometric redshift catalogue, where σ is an error for each photometric redshift estimation. The photometric redshifts of galaxies are compared with spectroscopical data (Hughes et al. 1995; Munn et al. 1997; Hughes & Birkinshaw 1998). The mean difference between spectroscopic redshift $z_{\rm spec}$ and photometric redshift

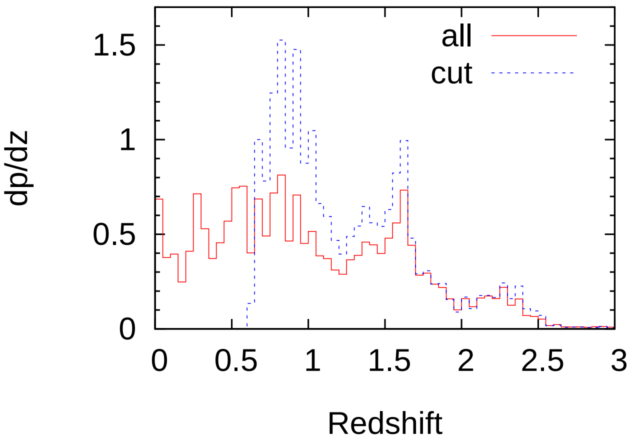

Figure 2. Photometric redshift distributions of galaxies. Solid and dotted lines show the distribution for all galaxies and background galaxies defined by $z_{\rm photo} - \sigma \geqslant 0.6$, respectively.

is $z_{\rm photo} - z_{\rm spec} \sim 0.004$. Our photometric redshifts tend to be underestimated for galaxies with $V - i' \sim 1.5$ about $\Delta z \sim -0.1$ (Kodama et al. 1999). In order to investigate the effect of this tendency, we estimate lensing signals with several different redshift selection criteria. However, we do not find any significant change of our result.

We use the code *Lensfit* (Miller et al. 2007; Kitching et al. 2008; Miller et al. 2013) for estimating the lensing signals. Lensing signals are estimated with the i'-band mosaic data. We choose 40×40 pixel^2 as a postage stamp size in order to estimate galaxy ellipticities with *Lensfit*. To eliminate galaxies that are not suitable for measuring lensing signals, e.g., blended galaxies, lensing signals are estimated with only galaxies with the flag $fitclass = 0$ in $Lensfit$. The total number of galaxies used for weak lensing analysis is $28,315$. For each galaxy, we assign a weight defined by (e.g., Miller et al. 2013)

$$w_{\rm g} = \left[\frac{\sigma_\varepsilon^2 \varepsilon_{\rm max}^2}{\varepsilon_{\rm max}^2 - 2\sigma_\varepsilon^2} + \sigma_{\rm pop}\right]^{-1}, \qquad (13)$$

where σ_ε is the one-dimensional variance in ellipticity of the likelihood surface, $\sigma_{\rm pop}$ is the one-dimensional variance of the distribution of ellipticity of the galaxy samples, and $\varepsilon_{\rm max}$ is the maximum allowed ellipticity. The reduced shear in the n-th bin is calculated with the weight as (Seitz & Schneider 1995; Bartelmann & Schneider 2001)

$$\langle {\rm g}_\mu \rangle (\theta_n) = \frac{\sum_{i=1}^{N_g} w_{{\rm g},i}\varepsilon_{\mu,i}}{\sum_{i=1}^{N_g} w_{{\rm g},i}}, \qquad (14)$$

where μ indicates tangential or cross shear components. The convergence value at each point is obtained with galaxy ellipticity as

$$\kappa(\boldsymbol{\theta}) = \frac{1}{{\rm n_g}\pi}\sum_i {\rm Re}\left[\tilde{\mathscr{D}}^*\left(\boldsymbol{\theta}-\boldsymbol{\theta}_i\right) w_{{\rm g},i}\varepsilon_i\right] / \sum_i w_{{\rm g},i}, \qquad (15)$$

where ${\rm n_g}$ is a number density of galaxies, and $\tilde{\mathscr{D}}$ is the kernel defined as

$$\tilde{\mathscr{D}}\left(\boldsymbol{\theta}\right) = \left[1 - \left(1 + \frac{|\boldsymbol{\theta}|^2}{\theta_{\rm s}^2}\right)\exp\left(-\frac{|\boldsymbol{\theta}|^2}{\theta_{\rm s}^2}\right)\right]\mathscr{D}(\boldsymbol{\theta}), \qquad (16)$$

where $\theta_{\rm s}$ is a smoothing scale. The statistical error in the shear measurement for each bin is computed from the weighted average of the variance of the shear $\sigma_{\rm g}^2$ (see Okabe et al. 2010; Oguri et al. 2012). For this purpose, we identify 20 neighboring galaxies in the magnitude-galaxy scale length plane. The variance, which is defined as $\sigma_{\rm g}^2 = \sigma_{\rm g1}^2 + \sigma_{\rm g2}^2$, is computed over the neighboring samples. Using the statistical error of shear for the i-th galaxy $\sigma_{{\rm g},i}$, the uncertainty on the tangential shear in each bin is estimated with the weight as

$$\sigma_{\rm g+}^2\left(\theta_n\right) = \frac{1}{2}\frac{\sum_i w_{{\rm g},i}^2\sigma_{{\rm g},i}^2}{\left(\sum_i w_{{\rm g},i}\right)^2}. \qquad (17)$$

The factor $1/2$ accounts for the fact that $\sigma_{{\rm g},i}$ is the rms for sum of two distortion components. We assume that the correlation between different bins is negligibly small, i.e., the main source of the statistical error comes from the intrinsic ellipticities.

In order to quantify the significance of the filament detection, we estimate the difference of the profiles from a null profile, i.e., ${\rm g}_{+,{\rm ana}}(\theta_i) = 0$ in equation (12). We estimate the significance by comparing the estimated chi-square values with the chi-square distribution. In this paper, we use filament shear profiles up to 15 arcmin.

In the shear measurement, we select galaxies in the photometric redshift range $z - \sigma \geqslant 0.6$ and estimate the lensing depth for the galaxies with equation (4). The value of the lensing depth $\langle {\rm D_{ls}}/{\rm D_s}\rangle$ is 0.419. Figure 2 shows the redshift distribution of galaxies.

3.2 Estimation of the effect of the clusters

First, we select the Brightest Cluster Galaxy for each cluster (hereafter BCG) and define a line connecting both BCG positions, which we call BCG-BCG axis. Then, we define a filament region, which are the region between both BCGs and outside a radius ${\rm R}_i$ from each BCG (shaded region in Figure 3). The filament length l is defined on the sky plane as

$$L_{\rm 2D} = \sum_i {\rm R}_i + l, \qquad (18)$$

where $L_{\rm 2D}$ is the distance between both BCG positions and the index labels the clusters. As explained in Section 2.2, shear profiles of the filament region is calculated as a function of distance from the BCG-BCG axis.

Since lensing signals from filaments are weak, clusters at both edges of the filament can affect lensing signals of the filament significantly. Therefore, it is important to subtract such cluster contributions. In order to subtract the effect, we estimate a background which comes from cluster weak lensing signals, and subtract the background from the lensing signals in the filament region. The background is estimated with two different methods to check robustness against background subtraction methods. The first method uses analytical profiles of the clusters. The second method estimates the background from the opposite sides of the filaments. Figure 3

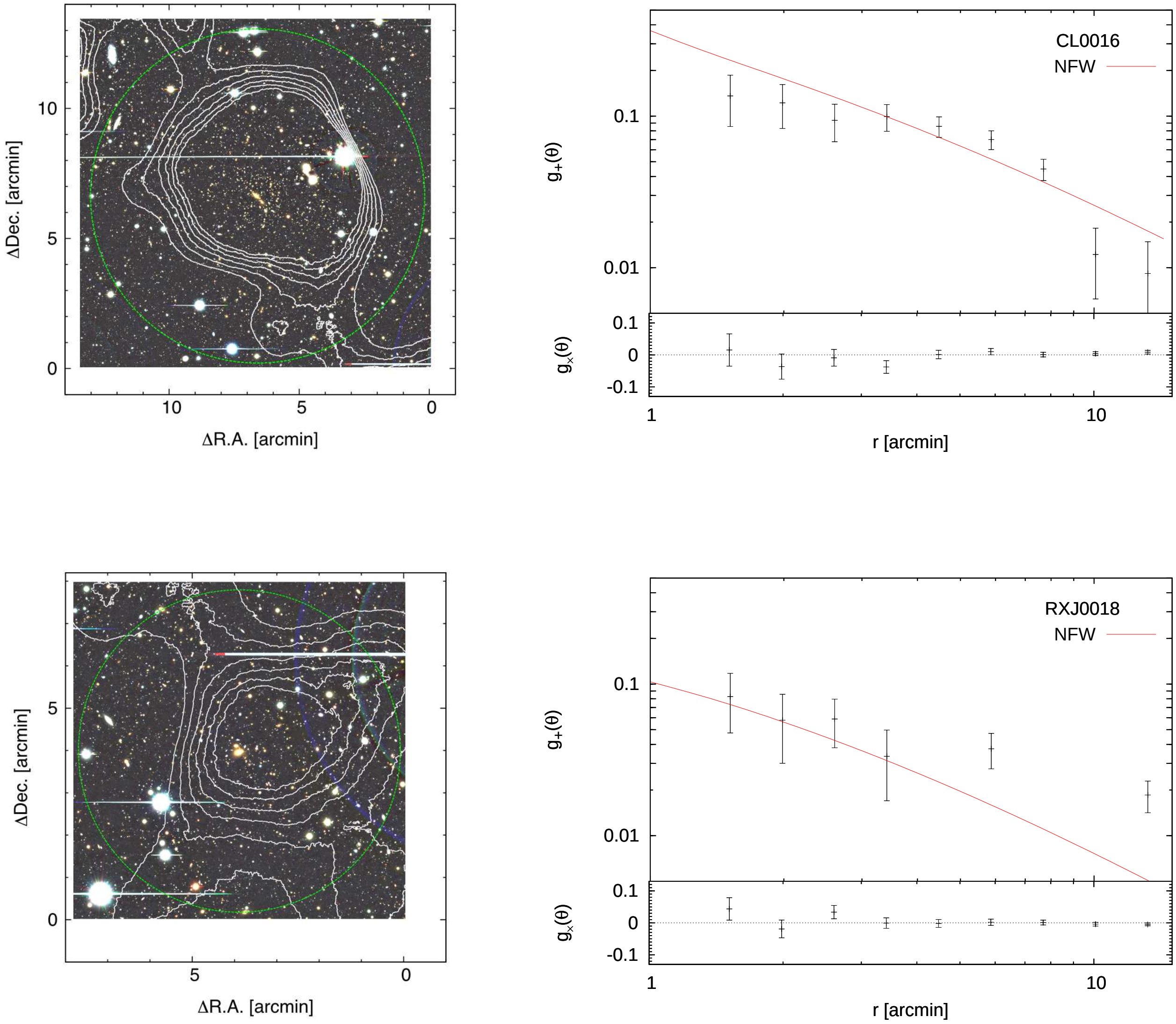

Figure 4. Left panels show the Subaru/Suprime-Cam image and contours of the convergence field for CL0016 (upper) and RX J0018 (lower). The contours (solid line) show the significance above the mean of the field edge spaced in a unit of 0.5σ from 0.5σ up to 3σ for clarity. The dashed circles indicate the viral radii estimated from the shear profile fitting in Section 3. Right panels show the radial profiles of tangential and cross shear as a function of distance from the each BCG position. The error bars show the 1σ measurement errors. The solid lines show the best-fit NFW profiles. In the tangential shear profile for RX J0018, the values of the fifth, seventh and eighth bins are not displayed due to low values.

illustrate the procedure which we explained in this subsection.

3.2.1 *Subtracting the analytical profiles*

The first background subtraction method is to subtract cluster lensing signals estimated from the best-fit analytical model. Assuming that the lensing signals of the clusters are well modeled with the spherically symmetric NFW profile, the effects from both clusters to the lensing signals of the filament region can be removed by subtracting the lensing signals constructed with the best-fit NFW models.

We fit tangential shear profiles of both clusters with the NFW profile by minimizing chi-square values defined in equation (12). Figure 4 shows the tangential shear profiles and the best-fit NFW profiles. The best-fit parameters are $\mathrm{M_{vir}} = \left(2.09^{+0.10}_{-0.21}\right) \times 10^{15} h^{-1} \mathrm{M_\odot}$ and $\mathrm{c_{vir}} = 5.56^{+0.63}_{-0.79}$ for CL0016, and $\mathrm{M_{vir}} = \left(4.51^{+1.13}_{-1.05}\right) \times 10^{14} h^{-1} \mathrm{M_\odot}$ and $\mathrm{c_{vir}} = 4.61^{+1.90}_{-1.35}$ for RX J0018. The best-fit masses are consistent with the results obtained from the X-ray observations (Hughes et al. 1995; Solovyeva et al. 2007). The two-dimensional lensing shear maps of the clusters are constructed with these parameters. Then, for each background

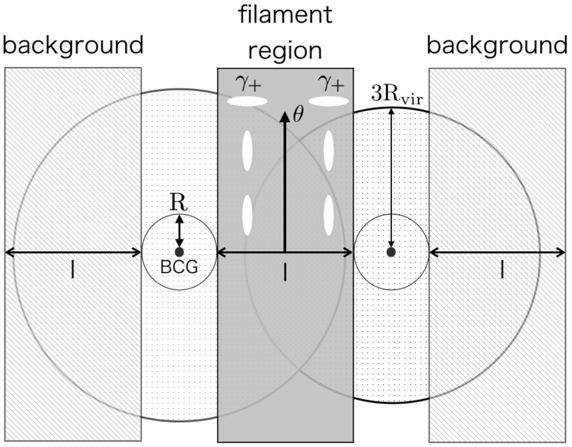

Figure 3. Definition of the regions and explanation for the background estimation. The black points show the locations of BCGs. A region between clusters and outside R from each BCG are defined as the filament region (shaded region). In the first method for a background estimation, shear profiles inside $3\mathrm{R}_{\mathrm{vir}}$ from BCGs (dotted regions) are estimated with the analytical models and subtracted. In the second method, the regions on the side opposite to the filament, where regions inside R from the each BCG are excluded, are defined as background (striped regions). Ellipses in the filament region indicate the distorted directions of images of background galaxies by a mass distribution of the filament.

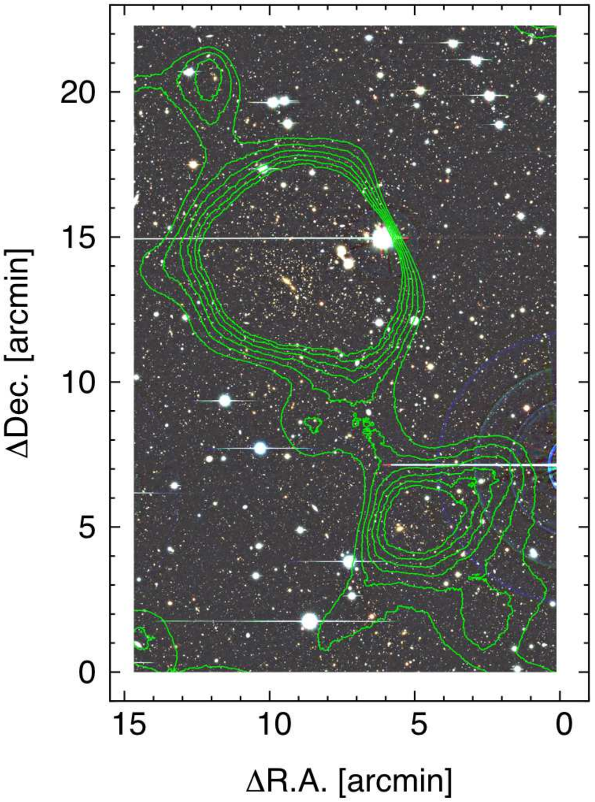

Figure 5. The mass map reconstructed with weak lensing. The cluster near the centre is CL0016. RX J0018 is located on the lower-right corner. The contours show significance above the mean of the field edge spaced in a unit of 0.5σ from 0.5σ.

galaxies inside $3\mathrm{R}_{\mathrm{vir}}$ from BCG positions shear values of the cluster components are subtracted to remove the cluster contribution. We also estimate the cluster masses only with galaxies which do not exist in the filament region. The estimated parameters are almost consistent within 1σ.

3.2.2 *Empirical background subtraction using opposite sides of the clusters*

The second background estimation method is to subtract the the shear profile on the opposite sides of the clusters. An advantage of this second approach is that it takes account of elongations of clusters which are ignored in the first method. As shown in Figure 3 (stripe region), the background is set to the same length as that of the filament length. The regions inside R_i from each BCG are excluded. Then, the tangential shear in the background is estimated as a function of distance from the line along the BCG-BCG axis, which is subtracted from the tangential shear profile in the filament region to obtain the final profile.

4 RESULT

Figure 5 shows the convergence map. We find the mass bridge between CL0016 and RX J0018, which is also seen in the galaxy distribution (Figure 1).

Figure 6 shows the tangential and cross shear profiles of the filament for both background subtraction methods. The shear profiles are shown for different definitions of the excluded region ($\mathrm{R} = 1/4\mathrm{r}_{\mathrm{vir}}$, $1/2\mathrm{r}_{\mathrm{vir}}$ and $3/4\mathrm{r}_{\mathrm{vir}}$) to check the sensitivity of our results on the size of the excluded region. We find that the tangential shear profiles are similar to the shear profile expected from the convergence profile in equation (6) (see also Higuchi et al. 2014), whereas B-mode profiles are consistent with zero for both background subtraction methods. Table 1 summarizes the values of the significances for the tangential shear profiles up to 15 arcmin for different definitions of the excluded region, estimated from χ^2 for the null shear profile. We find that the filament profiles are detected at the significance $\gtrsim 2\sigma$ for the case of empirical background subtraction method. For the analytical background subtraction method, the detection significances are much higher, but B-mode profiles in the inner region slightly deviates from zero, which may indicate insufficient background subtraction due to the aspherical profiles of the clusters. To illustrate this point, we compute the detection significances also for the B-mode (cross) shear profiles, which are summarized in Table 2. While the χ^2 values are consistent with those expected from the χ^2 distribution for the empirical background subtraction method, χ^2 values are significantly larger than expected for the analytical background subtraction method, suggesting significant residuals for the analytical background subtraction.

We also check the dependence of the profiles on the size of bins and the selection of galaxies. For instance, we change the size of bins and change the photometric cut to $z_{\mathrm{photo}} - \sigma \geqslant 0.7$ or $z_{\mathrm{photo}} - \sigma \geqslant 0.8$. However, these changes do not strongly affect our result.

We also estimate the average projected mass of the fila-

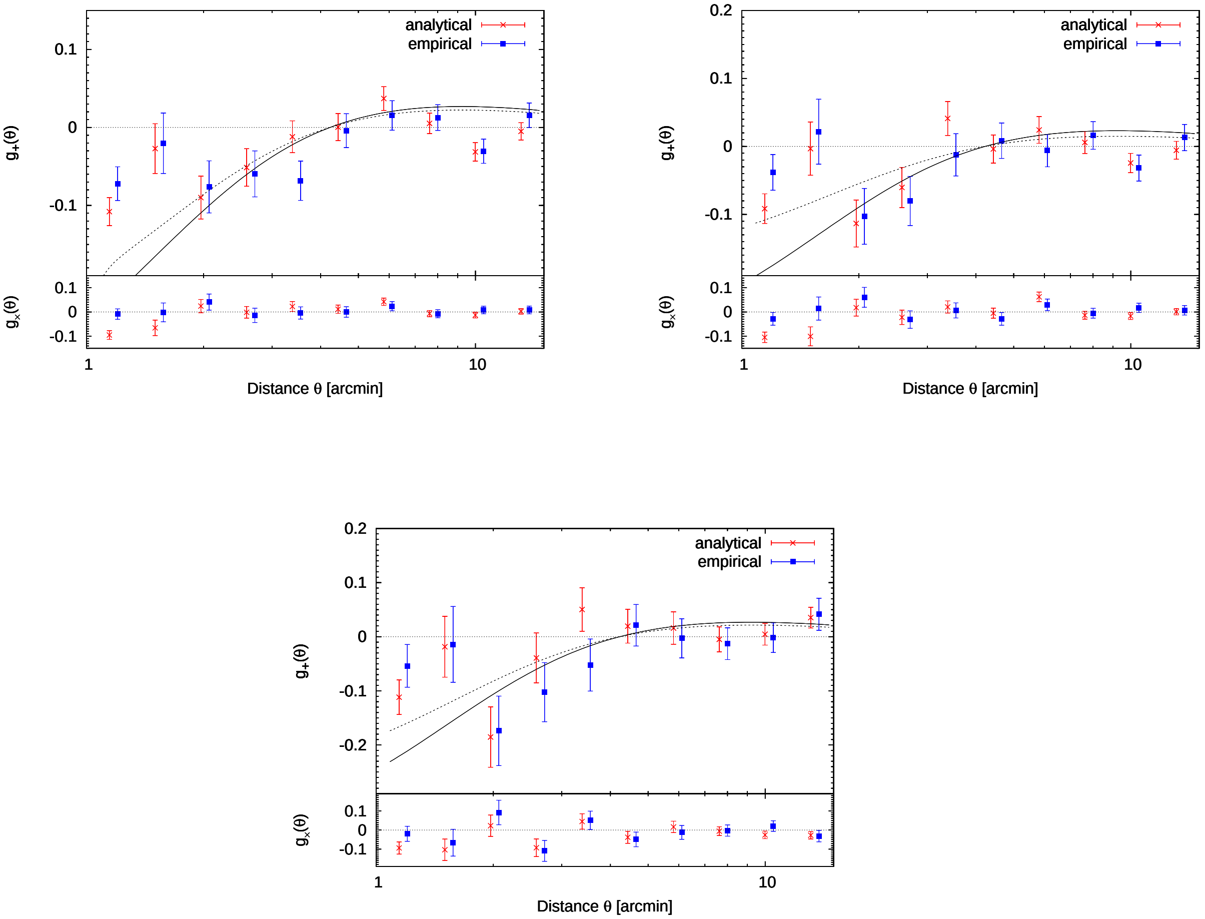

Figure 6. Tangential profiles of the filament for different excluded regions (*upper left*: $1/4\mathrm{r_{vir}}$; *upper right*: $1/2\mathrm{r_{vir}}$; *lower*: $3/4\mathrm{r_{vir}}$). The crosses show the values estimated with the analytical background subtraction method. The squares show the values for the empirical background subtraction method. The error bars show 1σ. The solid and dotted lines show the best-fit profiles with $\theta_c = 2$ arcmin for the analytical and empirical background subtracted profiles.

Table 1. Significance for the tangential shear profiles up to 15 arcmin for different definitions of the excluded region. Column (1): background estimation method; Column (2)-(4): value of significance.

background subtraction method		size of the excluded region	
	$1/4\mathrm{r_{vir}}$	$1/2\mathrm{r_{vir}}$	$3/4\mathrm{r_{vir}}$
analytical model	13.5σ	7.36σ	4.91σ
empirical	5.95σ	2.05σ	1.75σ

Table 2. Similar to Table 1. But for the cross shear profiles. Column (1): background estimation method; Column (2)-(4): value of significance.

background subtraction method		size of the excluded region	
	$1/4\mathrm{r_{vir}}$	$1/2\mathrm{r_{vir}}$	$3/4\mathrm{r_{vir}}$
analytical model	8.29σ	8.10σ	3.30σ
empirical	1.11σ	0.25σ	0.65σ

Table 3. Average projected mass density of the filament. The mass density is estimated with convergence values within 3 arcmin from the BCG-BCG line for each definition of the excluded region. The errors indicate 1σ error.

Definition of the excluded region	$1/4\mathrm{r}_{\mathrm{vir}}$	$1/2\mathrm{r}_{\mathrm{vir}}$	$3/4\mathrm{r}_{\mathrm{vir}}$
Projected mass density $[10^{14}h\mathrm{M}_{\odot}/\mathrm{Mpc}^2]$	3.23 ± 0.10	3.21 ± 0.10	3.20 ± 0.10

Table 4. Best-fit parameters with $\theta_c = 2$ arcmin. Column (1): background estimation method; Column (2)-(4): value of κ_0.

background subtraction method	size of the excluded region $1/4\mathrm{r}_{\mathrm{vir}}$	$1/2\mathrm{r}_{\mathrm{vir}}$	$3/4\mathrm{r}_{\mathrm{vir}}$
analytical model	0.33	0.29	0.33
empirical	0.28	0.19	0.27

ment from the convergence map, using convergence values up to $\theta_0 = 3$ arcmin from the BCG-BCG axis. Here we use the convergence map before the background subtraction. Table 3 shows the average and error of projected mass density for different excluded regions. We find that the value of the projected mass density is almost consistent with previous weak lensing studies of filaments (Dietrich et al. 2012; Jauzac et al. 2012). We fit the tangential shear profiles with the analytical profile defined with equation (6). For simplicity, we fix $\theta_c = 2$ arcmin. Table 4 shows the best-fit values for κ_0. Table 5 shows the projected mass within 3 arcmin from the BCG-BCG axis, which are estimated by equation (6) with the best-fit parameters. The estimated mass densities are higher than those estimated from the convergence values that are estimated from the smoothed mass map. The fitting with the fixed parameter θ_c might also be a part of reasons for this discrepancy.

5 CONCLUSION

In this paper, we have investigated the weak lensing properties of a filament between the cluster CL0015.9+1609 and RX J0018.3+1618 with the Subaru/Suprime-Cam data. We have selected background galaxies with photometric redshift and estimated the lensing signals with *Lensfit*. We have subtracted the effects of the clusters from the lensing profile of the filament with two different methods. One is to subtract the best-fit NFW profiles, and the other is to subtract the profile obtained on the opposite sides of the filament.

We have fitted the tangential shear profiles of the clusters with the NFW model, and obtained $\mathrm{M}_{\mathrm{vir}} = \left(2.09^{+0.10}_{-0.21}\right) \times 10^{15}h^{-1}\mathrm{M}_{\odot}$ and $\mathrm{c}_{\mathrm{vir}} = 5.56^{+0.63}_{-0.79}$ for CL0016, and $\mathrm{M}_{\mathrm{vir}} = \left(4.51^{+1.13}_{-1.05}\right) \times 10^{14}h^{-1}\mathrm{M}_{\odot}$ and $\mathrm{c}_{\mathrm{vir}} = 4.61^{+1.90}_{-1.35}$ for RX J0018. The estimated viral radii are used to define the size of the excluded regions.

We have found the mass bridge between two clusters on the convergence map. We have estimated the average surface mass density for three different excluded region definitions. The surface mass density for the excluded region definition of $\mathrm{R} = 3/4\mathrm{r}_{\mathrm{vir}}$ is found to $(3.20 \pm 0.10) \times 10^{14}h\mathrm{M}_{\odot}\mathrm{Mpc}^{-2}$ from the convergence map. This is consistent with previous studies of filaments.

We have derived the shear profiles of the filament using different excluded region definitions and background subtraction methods. For all the definitions of the excluded region, we have found that the cross shear values are almost consistent with zero and tangential shear profiles have same profiles as those expected from simulations, indicating that the lensing signals of the filament are detected. We have compared the shear profiles with a null profile up to 15 arcmin from the BCG-BCG axis to find that the lensing signals of the filament are detected at the significance $\gtrsim 2\sigma$ in all cases.

The detection of filaments with weak gravitational lensing is difficult due to small values of lensing signals. However, large-scale surveys such as Hyper Suprime-Cam and Large Synoptic Survey Telescope may enable direct observations of more filaments. Statistics of weak lensing properties of filaments therefore serve as a new test of structure formation in the Universe (Higuchi et al. 2014).

ACKNOWLEDGEMENTS

We would like to thank Takashi Hamana, Satoshi Miyazaki, Yuki Okura and Junko Ueda for useful discussion. We would like to thank Tadayuki Kodama for providing the photo-z catalogue. Data analysis were carried out on common use data analysis computer system at the Astronomy Data Center, ADC, of the National Astronomical Observatory of Japan. Based on data collected at Subaru Telescope and obtained from the SMOKA, which is operated by the Astronomy Data Center, National Astronomical Observatory of Japan. This work was supported in part by the FIRST program Subaru Measurements of Images and Redshifts (SuMIRe), World Premier International Research Center Initiative (WPI Initiative), MEXT, Japan, and Grant-in-Aid for Scientific Research from the JSPS (26800093), and in part by Grant-in-Aid for Scientific Research from the JSPS Promotion of Science (23540324, 23740161).

REFERENCES

Aragon-Calvo M. A., Yang L. F., 2014, MNRAS, 440, L46

Table 5. Projected mass density of the filament estimated by equation (6) with the best-fit parameter. The masses within 3 arcmin from the BCG-BCG axis are calculated with $\theta_c = 2$ arcmin. The error indicates 1σ error. Column (1): background estimation method; Column (2)-(4): projected mass for each excluded region definition.

background subtraction method	projected mass density [$10^{14} h \mathrm{M}_\odot/\mathrm{Mpc}^2$]		
	$1/4\mathrm{r}_{\mathrm{vir}}$	$1/2\mathrm{r}_{\mathrm{vir}}$	$3/4\mathrm{r}_{\mathrm{vir}}$
analytical model	$6.82^{+0.09}_{-0.09}$	$5.89^{+0.11}_{-0.12}$	$6.82^{+0.16}_{-0.16}$
empirical	$5.68^{+0.12}_{-0.13}$	$3.82^{+0.15}_{-0.17}$	$5.47^{+0.20}_{-0.21}$

Baba H. et al., 2002, in Astronomical Society of the Pacific Conference Series, Vol. 281, Astronomical Data Analysis Software and Systems XI, Bohlender D. A., Durand D., Handley T. H., eds., p. 298

Bartelmann M., Schneider P., 2001, Physical Rep., 340, 291

Bertin E., Arnouts S., 1996, A&AS, 117, 393

Blake C., Bridle S., 2005, MNRAS, 363, 1329

Bond J. R., Kofman L., Pogosyan D., 1996, Nat, 380, 603

Briel U. G., Henry J. P., 1995, A&A, 302, L9

Clampitt J., Jain B., Takada M., 2014, preprint (arXiv:1402.3302)

Clowe D. et al., 1998, ApJ, 497, L61

Codis S. et al., 2012, MNRAS, 427, 3320

Colberg J. M., Krughoff K. S., Connolly A. J., 2005, MNRAS, 359, 272

Connolly A. J. et al., 1996, ApJ, 473, L67

Dietrich J. P. et al., 2004, in IAU Colloq. 195: Outskirts of Galaxy Clusters: Intense Life in the Suburbs, Diaferio A., ed., pp. 34–38

Dietrich J. P. et al., 2012, Nat, 487, 202

Durret F. et al., 2003, A&A, 403, L29

Fang T. et al., 2002, ApJ, 572, L127

Furlanetto S. R., Piran T., 2006, MNRAS, 366, 467

Gao L. et al., 2008, MNRAS, 387, 536

Gavazzi R. et al., 2004, A&A, 422, 407

Gray M. E. et al., 2002, ApJ, 568, 141

Heymans C. et al., 2008, MNRAS, 385, 1431

Higuchi Y., Oguri M., Hamana T., 2013, MNRAS, 432, 1021

Higuchi Y., Oguri M., Shirasaki M., 2014, MNRAS, 441, 745

Hikage C. et al., 2008, MNRAS, 389, 1439

Hinshaw G. et al., 2013, ApJS, 208, 19

Hughes J. P., Birkinshaw M., 1998, ApJ, 497, 645

Hughes J. P., Birkinshaw M., Huchra J. P., 1995, ApJ, 448, L93

Hütsi G., 2006, A&A, 459, 375

Jauzac M. et al., 2012, MNRAS, 426, 3369

Kaiser N. et al., 1998, preprint (arXiv:astro-ph/9809268)

Kamionkowski M., Verde L., Jimenez R., 2009, JCAP, 1, 10

Kitching T. D. et al., 2008, MNRAS, 390, 149

Kodama T., Bell E. F., Bower R. G., 1999, MNRAS, 302, 152

Kodama T. et al., 2005, PASJ, 57, 309

Krause E. et al., 2013, ApJ, 762, L20

Marín F. A. et al., 2013, MNRAS, 432, 2654

Martinez V., Saar E., 2002, in Society of Photo-Optical Instrumentation Engineers (SPIE) Conference Series, Vol. 4847, Society of Photo-Optical Instrumentation Engineers (SPIE) Conference Series, Starck J.-L., Murtagh F. D., eds., pp. 86–100

Mead J. M. G., King L. J., McCarthy I. G., 2010, MNRAS, 401, 2257

Miller L. et al., 2013, MNRAS, 429, 2858

Miller L. et al., 2007, MNRAS, 382, 315

Miyazaki S. et al., 2002, PASJ, 54, 833

Munn J. A. et al., 1997, ApJS, 109, 45

Navarro J. F., Frenk C. S., White S. D. M., 1997, ApJ, 490, 493

Oguri M. et al., 2012, MNRAS, 420, 3213

Okabe N. et al., 2010, PASJ, 62, 811

Petri A. et al., 2013, Phys. Rev. D, 88, 123002

Planck Collaboration et al., 2013, preprint (arXiv:1303.5076)

Planck Collaboration et al., 2015, preprint (arXiv:1502.01589)

Rest A. et al., 2014, ApJ, 795, 44

Seitz C., Schneider P., 1995, A&A, 297, 287

Sheth R. K., Jain B., 2003, MNRAS, 345, 529

Solovyeva L. et al., 2007, A&A, 476, 63

Sousbie T. et al., 2008, MNRAS, 383, 1655

Sousbie T. et al., 2006, preprint (arXiv:0602628)

Springel V., 2005, MNRAS, 364, 1105

Sutter P. M. et al., 2015, MNRAS, 446, L1

Tanaka M. et al., 2009, A&A, 505, L9

Tanaka M. et al., 2005, MNRAS, 362, 268

Tegmark M. et al., 2006, Phys. Rev. D, 74, 123507

Tittley E. R., Henriksen M., 2001, ApJ, 563, 673

Werner N., 2008, PhD thesis, Utrecht University

Wright C. O., Brainerd T. G., 2000, ApJ, 534, 34